

Monodispersed Ce(IV)–Gd(III)–Eu(III) oxide phosphors for enhanced red emission under visible excitation†

Cite this: *J. Mater. Chem. C*, 2014, 2, 1010

C. Sorbello,^a B. C. Barja^{*ab} and M. Jobbágy^{*abc}

A family of $\text{Ce}_{0.95-x}\text{Gd}_x\text{Eu}_{0.05}(\text{OH})\text{CO}_3 \cdot \text{H}_2\text{O}$ monodispersed spherical particles of ca. 200 nm with $0 \leq x \leq 0.95$ was obtained by the urea homogeneous alkalinization method. These precursors were decomposed at 1273 K under an air atmosphere, resulting in ternary spheroidal phosphors obeying the general formula $\text{Ce}_{0.95-x}\text{Gd}_x\text{Eu}_{0.05}\text{O}_{1.975-x/2}$. Samples with $0.57 \leq x \leq 0.95$ exhibit a c-type (*la3*) structure related to the Gd_2O_3 lattice, while a $Fm\bar{3}m$ -type (CeO_2) one was found for $0 \leq x \leq 0.19$. For both ternary families, the partial substitution of host cations dramatically decreases the efficiency of the ligand to metal charge transfer (LMCT) based emission, with respect to their binary end members. In contrast, the emission obtained from direct excitation of Eu(III) with visible light is enhanced. For both structures, the binary Ce(IV)–Gd(III) host improved emission with respect to $\text{Gd}_{0.95}\text{Eu}_{0.05}\text{O}_{1.5}$ and $\text{Ce}_{0.95}\text{Eu}_{0.05}\text{O}_{1.975}$ samples, achieving an optimum value for the sample $\text{Ce}_{0.23}\text{Gd}_{0.71}\text{Eu}_{0.05}\text{O}_{1.6}$ with a *la3* structure.

Received 4th October 2013
Accepted 18th November 2013

DOI: 10.1039/c3tc31952k

www.rsc.org/MaterialsC

Introduction

Nowadays, inorganic phosphorescent materials are triggering an increasing number of applications beyond the traditional ones related to luminescent display technology. New soft chemistry based synthetic routes have allowed the preparation of many of these phosphors in the form of sub-micrometric or even nanoparticles, opening the gate for their application in bio labeling. Among them, trivalent rare earth (RE)-based oxides arise as a suitable alternative due to their highly biocompatible chemical nature.¹ In particular, europium-based phosphors hosted in RE_2O_3 oxides are currently employed as a non-bleachable source of red photons, due to their characteristic sharp emissions centered at 610 nm, arising from the Eu(III) $^5\text{D}_0$ to $^7\text{F}_2$ intra-4f electronic transitions.^{2,3} One of the most accepted Eu(III) phosphors is based on the isomorphic substitution of this ion within the Y_2O_3 oxide; however binary $\text{Y}_{2-x}\text{Gd}_x\text{O}_3$ oxides arise as improved hosts since Gd(III) additionally plays the role of a magnetic resonance imaging contrast agent while preserving good emissive properties.^{4,5} In parallel, CeO_2 based RE phosphors demonstrate outstanding biocompatibility.^{6–8} Then, it is attractive to envisage binary oxidic nanoparticles based on Gd(III) and Ce(IV) to host RE based emissive centers. On these oxidic matrices, emission can be activated either

by UV excitation *via* the charge transfer (CT) band of the host oxide or by direct excitation of the Eu(III) active center, by means of visible range photons. In the case of the latter, an increasing number of appropriate excitation sources such as the GaN-LED (440–470) or the Kr–Ar laser (488 nm) expand the potential applications of these non-bleachable phosphors for biolabeling.^{2,9} Besides the inherent aspects of emission, mainly governed by the host's composition,¹⁰ the performance of luminescent particles also requires well tuned morphological properties (size, shape and monodispersion) as well as chemical homogeneity.^{11–14} In this sense, the urea method provides a powerful tool to prepare numerous precursors of mixed oxides, including several binary RE oxides¹⁰ in the form of monodispersed sub-micrometric spherical particles.^{15–18} Interestingly, beyond the RE_2O_3 phases, this method also allows the preparation of binary Ce(IV)–RE(III) oxides, using Ce(III) based precursors. This cation shares similar hydrolytic properties with most RE(III) ions, including Gd(III) and Eu(III), increasing the ability to develop coprecipitation of suitable precursors of the aforementioned cations.^{19,20} The present work presents a systematic preparation and exploration of a family of ternary phosphors obeying the general formula $\text{Ce}_{0.95-x}\text{Gd}_x\text{Eu}_{0.05}\text{O}_{1.975-x/2}$ with $0 \leq x \leq 0.95$, textured in the form of monodispersed sub-microparticles. The luminescent properties of the resulting phosphors are discussed in terms of their structure.

Experimental

Synthesis and characterization of precursors and their mixed oxides

Solutions containing Gd(III), Ce(III) and Eu(III) nitrates in a total amount of $5 \times 10^{-3} \text{ mol dm}^{-3}$ and urea 0.5 mol dm^{-3} were

^aDQIAQF, Facultad de Ciencias Exactas y Naturales, Universidad de Buenos Aires, Pabellón II, Ciudad Universitaria, C1428EHA-Buenos Aires, Argentina

^bINQUIMAE, CONICET, Argentina. E-mail: barja@qi.fcen.uba.ar

^cCentro Interdisciplinario de Nanociencia y Nanotecnología, Argentina. E-mail: jobbag@qi.fcen.uba.ar

† Electronic supplementary information (ESI) available: FESEM images and detailed PXRD patterns. See DOI: 10.1039/c3tc31952k

prepared by dissolving the salts in water. All solutions were made up using analytical grade reagents and deionized water (18 MΩ cm) obtained from a Milli-Q apparatus and filtered through 0.2 μm pore-size cellulose nitrate membranes.

The Eu(III) to total cationic content molar ratio was fixed at 5%. The Gd(III) to Ce(III) molar ratio was varied between 0 and 100 (see Table S1†). From now on, the samples will be named CGX, where $X = [\text{Gd(III)}]/([\text{Ce(III)}] + [\text{Gd(III)}])$. Typically, the precursor's precipitation experiments were performed as follows: 25 cm³ of filtered aliquots were poured into 30 cm³ screw-capped glass tubes, which were then placed in a thermostated water bath preheated at 363 K. After 3 h, the bottles were removed and immersed in an ice-water bath to quench the reaction. Precipitated solids were collected by filtration through 0.2 μm pore size cellulose nitrate membranes, washed three times with cold water, and dried at room temperature overnight. The supernatant solutions were stored for chemical analyses; Gd(III), Eu(III) and Ce(III) concentrations were determined, within ICP. The precursors' composition was assessed by CHON elemental analysis.

Mixed oxides (phosphors) were synthesized by heating precursors for 6 h at 1273 K under an air atmosphere. All synthesized solids were characterized by powder X-ray diffraction (PXRD) using the graphite-filtered CuK_α radiation ($\lambda = 1.5406 \text{ \AA}$), with a step size of 0.02 and 2 s step time. Cell parameters were estimated from the main reflections recorded between $20 < 2\theta < 100$ degrees.

High resolution scanning electron microscopy (HRSEM) coupled with Energy Dispersive X-ray Spectroscopy (EDS) was performed over samples straightly deposited onto conductive silicon wafer supports with no further metallization.

Characterization of luminescent properties of mixed oxides

The phosphors were grinded and introduced by pressing into quartz capillary tubes. The excitation and emission spectra were measured in a front face arrangement under the same conditions of thickness and slit widths. An OG515 Schott filter was employed in the emission to prevent the excitation beam from reaching the detector. The steady state emission spectra were recorded on a PTI QuantaMaster QM-1 luminescence spectrometer.

Results and discussion

In the aim of exploring the role of a Gd(III)–Ce(IV) matrix, a constant cationic fraction of Eu(III) fixed at 5% moles over the total cationic content was chosen. This load offers a good emission intensity and prevents the undesired non-radiative Eu(III) to Eu(III) energy transfer, according to previous reports dealing with related Eu_xRE_{2-x}O₃ matrices.⁵ Chemical analyses revealed that all precursors follow the formula Ce_{0.95-x}Gd_xEu_{0.05}(OH)CO₃·H₂O. PXRD inspection revealed an ill crystallized structure, exhibiting the typical broad diffraction signals of the so-called amorphous RE basic carbonates, in good agreement with the chemical composition (data not shown).^{19,21} Fig. 1 depicts HRSEM images of the typical monodispersed spherical particles of ca. 200 nm obtained; the size and shape

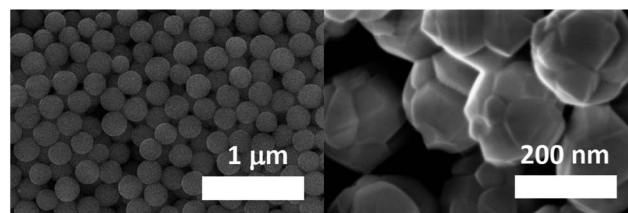


Fig. 1 FESEM images of a typical sample of amorphous Ce_{0.95-x}Gd_xEu_{0.05}(OH)CO₃·H₂O precursors (left) and the resulting spheroidal polycrystalline Ce_{0.95-x}Gd_xEu_{0.05}O_{1.975-x/2} phosphors obtained after thermal treatment (right).

were preserved irrespective of the Ce(III) to Gd(III) molar ratio. The precursors were decomposed in air at 1273 K in order to ensure a proper crystallization and chemical homogeneity in the phosphors, while preventing the undesired loss of primary texture due to the eventual sintering of the particles.^{22,23} After the annealing, the initially monodispersed precursor particles resulted in contracted 150 nm polycrystalline faceted spheroids; no major sintering was observed and the particles preserved their dispersibility (see Fig S1†).

PXRD of phosphors revealed the occurrence of two different yet related cubic cells (see Fig. 2).

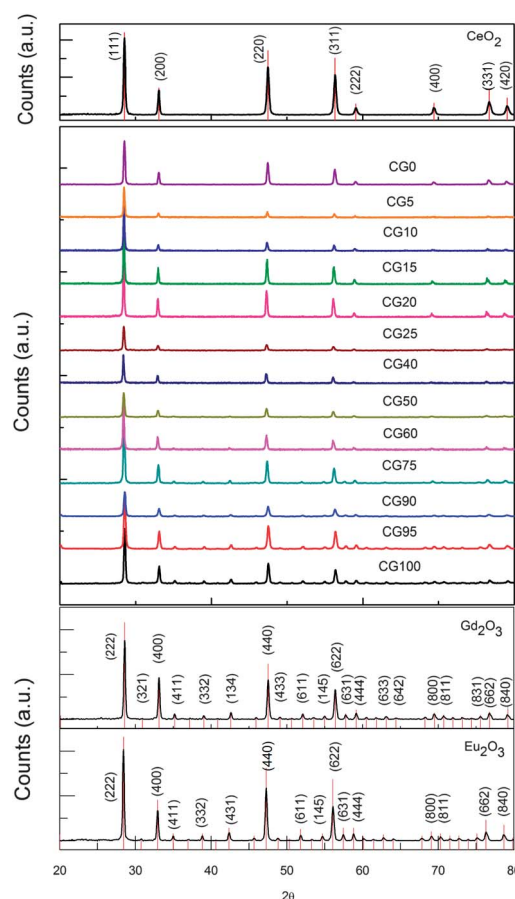


Fig. 2 Middle panel: PXRD patterns of the Ce_{0.95-x}Gd_xEu_{0.05}O_{1.975-x/2} phosphors. Indexed patterns of reference oxides Gd₂O₃; PDF#43-1014 and Eu₂O₃; PDF#34-0392 (lower panel), and CeO₂; PDF#65-2975 (upper panel), obtained under similar conditions.

For Gd(III)-rich samples, ranging from CG100 to CG50, reflections of the *c*-type (*Ia3* space group) phase related to bare Gd_2O_3 were observed, including characteristic 411, 332 and 134 reflections placed in the range of $34^\circ < 2\theta < 44^\circ$ (see Fig. S2†). For lower Gd(III) contents, all the reflections could be indexed to a CeO_2 -like structure ($Fm\bar{3}m$ space group). Fig. 3 presents the dependence of the cell parameter, either indexed to *Ia3* (RE_2O_3) or to $Fm\bar{3}m$, (REO_2) as a function of the Gd(III) to Ce(IV) molar ratio. Binary end members indicate that solid solutions with Eu(III) were achieved. The magnitude of lattice distortion of sample CG0 with respect to bare CeO_2 is fully coincident with previously reported Eu(III)–Ce(IV) solid solutions,^{24–26} and obeys the inherent differences between both cations' radii (see Table S2†) and the associated oxygen vacancies.²⁷ The CG100 cell also agrees with the value reported for $\text{Gd}_{1.9}\text{Eu}_{0.1}\text{O}_3$ solid solution, slightly expanded with respect to the parent Gd_2O_3 due to the larger radius of Eu(III) (see Table S2†).²⁸ Inspecting the whole range of compositions, three zones can be discriminated. Samples ranging from CG100 to CG60 exhibit a *Ia3* or *c*-type structure and their cells expand linearly with increasing Ce(IV) substitution, in excellent agreement with related reports (see Fig. S3†).²⁹ In contrast, samples ranging from CG0 to CG20 exhibiting a $Fm\bar{3}m$ cell expand linearly their *a* parameter with increasing Gd(III) contents. In this range, a solid solution is also expected; several trivalent RE cations, including Eu(III) and Gd(III), can be incorporated within the ceria lattice up to a cationic molar fraction of 0.25 with no *Ia3* phase segregation.^{30–34} Typically, under such conditions, the foreign trivalent cations are placed in sites with six, seven and eight-fold oxygen coordination environments within the CeO_2 lattice.^{35,36} A higher incorporation of RE(III) results in the enrichment of RE(III) dimers associated with oxygen vacancies³⁷ or even nanometric crystalline *Ia3* RE_2O_3 precipitates.³⁸ In the present case, samples with Gd(III) contents higher than sample CG20 and lower than sample CG60 exhibit a constancy in the *a* parameter. This intermediate compositional range can be interpreted in terms of a biphasic system in which a mixture of the aforementioned solid solutions coexists.

From the aforementioned results, the emissive properties of each monophasic family of samples will be analyzed separately, and a comparative discussion will be presented.

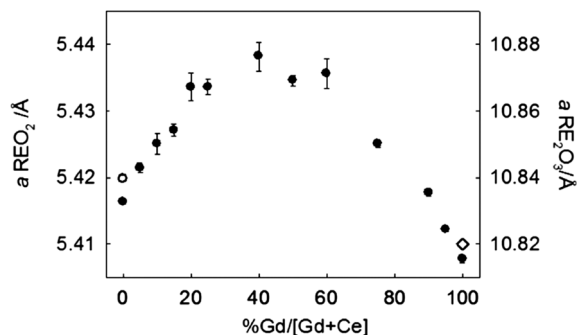


Fig. 3 Dependence of the cell parameter *a* as a function of the Gd(III) to Ce(IV) ratio; reference values for $\text{Gd}_{1.9}\text{Eu}_{0.1}\text{O}_3$ (◇, ref. 28) and $\text{Ce}_{0.95}\text{Eu}_{0.05}\text{O}_{1.975}$ (○, ref. 26) are also included.

Spectroscopic measurements

Structural correlations. An interesting and very useful property of the Eu(III) ions lies in the possibility of using them as structural probes given their capability to monitor the local environment in which they are located. This is so because the dielectric $^5\text{D}_0 \rightarrow ^7\text{F}_2$ (E) transition is known to be *hypersensitive*, and then greatly affected by the coordination environment in which the ion is immersed. On the other hand, the magnetic dipole transition $^5\text{D}_0 \rightarrow ^7\text{F}_1$ (M) is almost insensitive to the medium and can be used as an internal standard. In a site with inversion symmetry, the magnetic dipole transition $^5\text{D}_0 \rightarrow ^7\text{F}_1$ is dominant, while in a site without inversion symmetry the $^5\text{D}_0 \rightarrow ^7\text{F}_2$ electric dipole transition prevails.³⁹ The ratio of the aforementioned bands, *R*, provides an insight into the average symmetry of the Eu(III) environment.

Excitation spectra of CG0 and CG100

CG0 (CeO_2 host matrix). When Eu(III) ions are incorporated within the CeO_2 host lattice in loadings lower than 1%, they tend to isomorphically substitute Ce(IV) cations adopting a symmetrical O_h environment, reaching *R* values close to zero.^{40,41} In general, dopants with larger ionic radii than Gd(III), as is the case of Eu(III), tend to repel the oxygen vacancies at the next-nearest-neighbor (NNN) sites within the CeO_2 lattice.^{42–45} However, the *R* value can be affected by the annealing conditions.⁴⁶ It was also observed that for a given Eu(III) content, the value of *R* is lower when the matrix is excited at the LMCT band than when it is directly excited at the intra f–f bands of the dopant lanthanide.³⁰ For increasing concentrations of Eu(III), the emission efficiency through its direct excitation is enhanced up to contents of ca. 15–16%. In parallel, a dramatic rise in the *R* value occurs due to the increasing nearest-neighbor (NN) vacancies, obeying the massive depletion of oxygen ions in the lattice.^{9,46} Then, in addition to O_h sites at least three characteristic oxygen vacancy-compensated sites with C_{3v} , C_{2v} or lower symmetries define the emission spectra.⁴⁵ Fig. 4 shows the excitation spectra of CG0 measured at room temperature. The bands are assigned as follows: for the CG0 sample the broad band located at 366 nm corresponds to the LMCT band of $\text{Ce(IV)}_{4f}\text{O}_{2p}$. The $^7\text{F}_0 \rightarrow ^5\text{D}_2$ (E, electric) transition locates at 468 nm while the bands in the range 520 nm–540 nm correspond to the $^7\text{F}_{0,1} \rightarrow ^5\text{D}_1$ (M, magnetic) transitions of Eu(III).⁴⁷ The number of bands evidences that the environment of Eu(III)

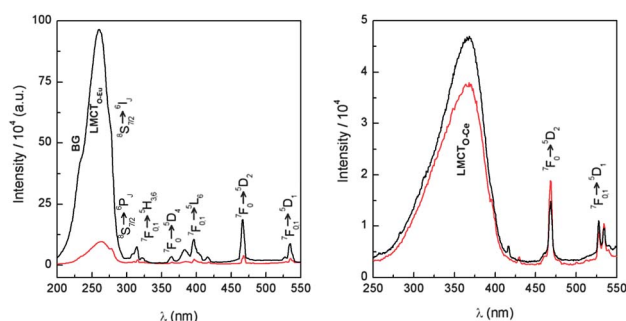


Fig. 4 Excitation spectra of CG100 (left) and CG0 (right) monitored at $\lambda_{\text{em}} = 610$ nm (black) and $\lambda_{\text{em}} = 590$ nm (red).

was distorted as a result of the interstitial Eu(III) and O^{2-} vacancy defects formed during charge compensation in the CeO_2 matrix with the Eu(III) ions being located in sites with lower symmetries. When the excitation spectra are monitored at 590 nm ($^5D_0 \rightarrow ^7F_1$, M), the intensity of the magnetic transitions enhances than when monitored at 612 nm ($^5D_0 \rightarrow ^7F_2$, E) allowing the identification of the nature of the transitions in the matrix. It is known that the band at 468 nm with $\Delta J = \pm 2$ is an electric dipole transition $^7F_0 \rightarrow ^5D_2$ and its intensity decreases when monitored at 590 nm. This can also be confirmed in the corresponding emission spectra.

The nature of the bands in the 525–535 nm range associated with the $^7F_{0,1} \rightarrow ^5D_1$ transitions of Eu(III) seems to be different. The low intensity band at 528 nm is enhanced when monitored at 590 nm in agreement with its magnetic nature while the intensities of the bands at 534 and 538 nm keep unaltered.

CG100 (Gd_2O_3 host matrix). Since Eu(III) and Gd(III) oxides are isostructural ($Ia3$ space group), once introduced into the latter phase, Eu(III) ions are able to isomorphically substitute Gd(III) ones developing a vacancy free solid solution. The foreign cation can either occupy the lattice centrosymmetric sites S_6 or the low symmetry sites C_2 which are present in a 1 : 3 ratio, respectively.⁴⁸ The S_6 sites have an inversion center and therefore only the magnetic transitions (M) are allowed according to the selection rules ($\Delta J = 0, \rightarrow 1$ with $J = 0 \rightarrow J = 0$ forbidden). In contrast, the C_2 sites allow electric dipole transitions (E), with $\Delta J = 0, \pm 1$ and ± 2 and either electric or magnetic transitions are allowed. The excitation spectra of CG100 (Fig. 4) were measured by monitoring the 5D_0 – 7F_2 (C_2) emission at 612 nm and at 590 nm. These spectra show the well-known sharp lines in the 300 nm to 550 nm region corresponding to the 4f–f transitions of Eu(III) and Gd(III). In the 300–320 nm range the $^7F_{0,1} \rightarrow ^5H_3/^5H_6$ transitions of Eu(III) overlap with the $^8S_{7/2} \rightarrow ^6P_J$ bands of the Gd(III) ion. The bands located at 394 nm, 468 nm and 360 nm correspond to the $^7F_{0,1} \rightarrow ^5L_6$, $^7F_0 \rightarrow ^5D_2$ (C_2) and $^7F_0 \rightarrow ^5D_4$ transitions of Eu(III) in this order. In the 500–550 nm range the bands of the $^7F_{0,1} \rightarrow ^5D_1$ transitions can be observed as well. The broad strong peak with maxima at 261 nm is assigned to the ligand to metal charge transfer band LMCT (O_{2p} – Eu_{4f}) while the shoulders located at 234 nm and at 276 nm correspond to the band gap of the CG100 and to the intra f–f transitions ($^8S_{7/2} \rightarrow ^6I_J$) of the Gd(III), respectively.

The band at 528 nm which is also present in the CG0 spectrum is assigned to a $^7F_0 \rightarrow ^5D_1$ (M) transition as discussed previously while the band at 534 nm should also be associated with the $^7F_0 \rightarrow ^5D_1$ transition but for sites of lower symmetry (C_2) in the matrix. Energy transfer from Eu(III) (C_2 site) to Eu(III) (S_6 site) occurs at room temperature because the energy difference between the 5D_0 levels of both ions can be bridged thermally.⁴⁸

From these spectra, it is clear that the excitation energy is transferred to the Eu(III) ions mostly through the LMCT (O_{2p} – Eu_{4f}), following the intra f–f transitions ($^8S_{7/2} \rightarrow ^6I_J$) of the Gd(III) and the band gap of CG100.

Emission spectra of CG0 and CG100. Fig. 5 shows the emission spectra of CG100 and CG0. The band assignment is as follows: 579 nm: $^5D_0 \rightarrow ^7F_0$ (E); 589 nm: ($^5D_0 \rightarrow ^7F_1$); 610 nm

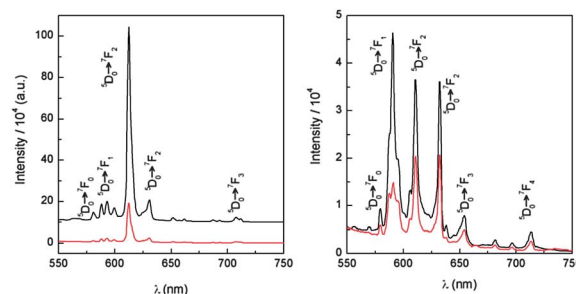


Fig. 5 Emission spectrum of CG100 (left) excited at 261 nm (black line) and at 468 nm (red line). Emission spectrum of CG0 (right) excited at 368 nm (black line) and at 468 nm (red line).

and 631 nm: ($^5D_0 \rightarrow ^7F_2$) and 653 nm: ($^5D_0 \rightarrow ^7F_3$).⁴¹ In pure ceria oxide the Ce(IV) ions occupy highly symmetric O_h sites (inversion center) and the selection rules dictate that only those transitions with $\Delta J = \pm 1$ (M) are allowed. No band associated with the electric $^5D_0 \rightarrow ^7F_2$ transition should be observed in a perfect O_h symmetry site but given the different charges between Eu(III) and Ce(IV) ions, the inclusion of the former introduces oxygen vacancies, relaxing the selection rules.⁴⁵ Fig. 5 shows that the magnetic $^5D_0 \rightarrow ^7F_1$ transition at 590 nm dominates the spectrum of CG0 over the electric dipole $^5D_0 \rightarrow ^7F_2$ bands at 610 and 630 nm (one band for $\Delta J = 1$ with the highest intensity and two bands for $\Delta J = 2$), indicating that the Eu(III) ions locate in sites with symmetry close to O_h . When the sample is excited at the LMCT band of $Ce(IV)_{4f}$ – O_{2p} (368 nm), the energy is transferred to the emissive state 5D_0 of the Eu(III) and the most intense emission occurs at 590 nm.

In contrast, when the Eu(III) is directly excited at the electric dipole transition $^7F_0 \rightarrow ^5D_2$ ($\lambda_{exc} = 468$ nm), the emission spectrum shows a different pattern because at this wavelength those transitions that are electrical in nature are being selected favoring the emission bands with $\Delta J = \pm 2$. The emission spectra of the Eu(III) ions in CG100 (Fig. 5) monitored at two different excitation wavelengths show the sharpest and most intense $^5D_0 \rightarrow ^7F_2$ (E) transition at 612 nm, together with another weaker one at 631 nm. The three 5D_0 – 7F_1 (M) transitions locate at 588, 590 and 600 nm while the 5D_0 – 7F_0 (E) locates at 581 nm. The intensity of the emission of these bands depends on the excitation wavelength in the following order.

$$I_{\lambda=261, \text{LMCT}(\text{Eu}_{4f}-\text{O}_{2p})} > I_{\lambda=276, \text{f-f of Gd(III)}} \gg I_{\lambda=234, \text{Band gap}} \cong I_{\lambda=466} > I_{\lambda=396}$$

This order shows that the energy transfer to the Eu(III) is most efficient exciting in the LMCT band (Eu_{4f} – O_{2p}). The assistance of the matrix in the emission spectra of the Eu(III) ions is evident if we compare them with the emission spectra obtained by direct excitation of the Eu(III) ions at 468 nm (E) (or 396 nm, not shown).

The number and profiles of the bands of the emission spectra of CG100 differ remarkably from those of CG0 (Fig. 5). In the emission spectrum of CG0, the electric dipole transition $^5D_0 \rightarrow ^7F_2$ (612 nm) of Eu(III) dominates the spectrum over the magnetic dipole transitions 5D_0 – 7F_1 (588, 593 and 600 nm) and the $^5D_0 \rightarrow ^7F_0$ transition at 581 nm. The bands at 612 nm and

631 nm of Eu(III) arise mainly from Eu(III) ions located in low symmetry C_2 sites ($\Delta J = \pm 2$) while the bands with $\Delta J = \pm 0, 1$ associated with the more symmetric S_6 sites are remarkably depressed.

Gd₂O₃-CeO₂ binary hosts

Excitation and emission spectra. Fig. 6 and 7 show how the incorporation of Ce(IV) into the Gd₂O₃ matrix drastically lowers the intensity of the LMCT ($O_{2p}-Eu_{4f}$) centered at 261 nm of CG100 to be replaced by the LMCT band of Ce(IV)_{4f}- O_{2p} .

This broad band gradually enhances and shifts from 322 nm (CG95) to 368 nm (CG0) overlapping the bands at 394 nm and 360 nm of the ${}^7F_{0,1} \rightarrow {}^5L_6$ and ${}^7F_0 \rightarrow {}^5D_4$ transitions of Eu(III) in this order. For most mixtures, the intensity of the LMCT band of Ce(IV)_{4f}- O_{2p} is always equal to or lower than the intensity of the intra f-f band of Eu(III) at 468 nm. These spectra indicate that in the mixtures, the excitation energy is not being efficiently transferred from the host to the Eu(III) emissive levels. The most luminescent emission spectrum is obtained by direct excitation of the Eu(III) ion at 468 nm for all the binary Ce(IV)-Gd(III) hosts (Fig. 8). The intensity of the band centered at 590 nm (${}^5D_0 \rightarrow {}^7F_1, M$) is equally relevant for the Ce(IV)-rich mixtures when the samples are excited at the LMCT band.

When the non-symmetric sites are selectively excited ($\lambda_{exc} = 468$ nm), R increases linearly with the gadolinium concentration indicating that the Eu(III) ions progressively locate in non-symmetrical environments (NN vacancies), either for the Ce(IV) or Gd(III) rich families.

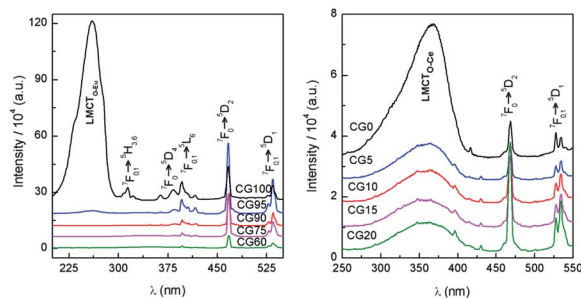


Fig. 6 Excitation spectra of Gd(III)-rich (left) and Ce(IV)-rich (right) samples monitored at 612 nm.

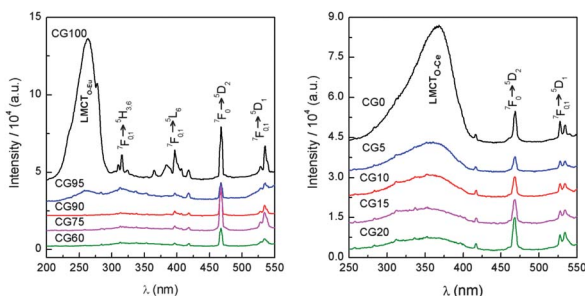


Fig. 7 Excitation spectra of Gd(III)-rich (left) and Ce(IV)-rich (right) samples monitored at 590 nm.

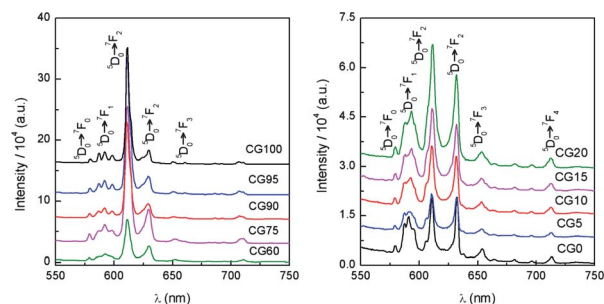


Fig. 8 Emission spectra of Gd(III)-rich (left) and Ce(IV)-rich (right) samples excited at 468 nm.

Fig. 9 shows the emission spectra of the mixtures excited at the LMCT bands, where all sites occupied by the Eu(III) ions are excited. The R value increases less markedly with the Gd(III) content because the more symmetric S_6 and O_h sites at which Eu(III) also locates tend to lower the value of R . Then, the ratio $R = (\lambda_{exc} = 468 \text{ nm})/R(\lambda_{exc} = \text{LMCT})$ would give a rough idea of the symmetry of the occupation sites in the mixtures.

Fig. 10 shows the variation of R with the Ce(IV) to Gd(III) molar ratio of the host matrix for $\lambda_{exc} = 466$ nm and 350 nm. Additionally, Fig. 11 shows the variation of the intensities of the

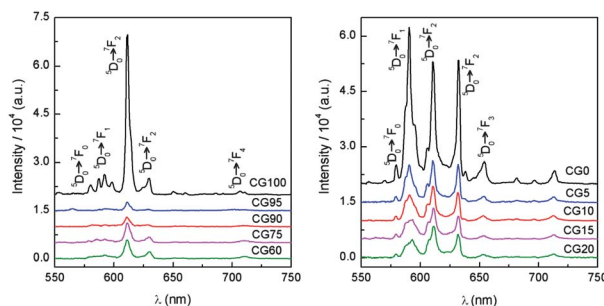


Fig. 9 Emission spectra of Gd(III)-rich (left) and Ce(IV)-rich (right) samples excited at the LMCT O-Ce band. CG100 was excited at 315 nm.

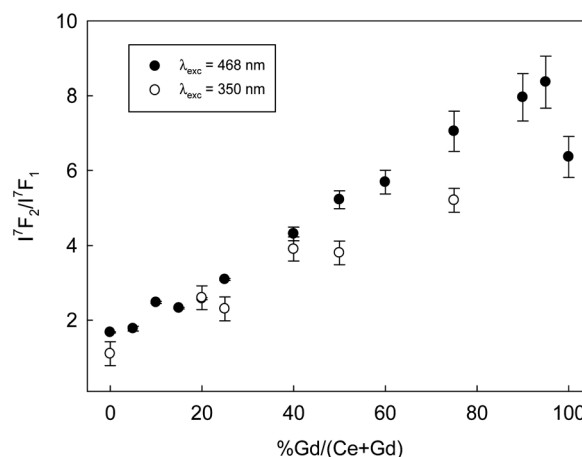


Fig. 10 Intensity ratio of Eu(III) ${}^5D_0 \rightarrow {}^7F_2$ and ${}^5D_0 \rightarrow {}^7F_1$ emission bands as a function of host composition and excitation wavelength.

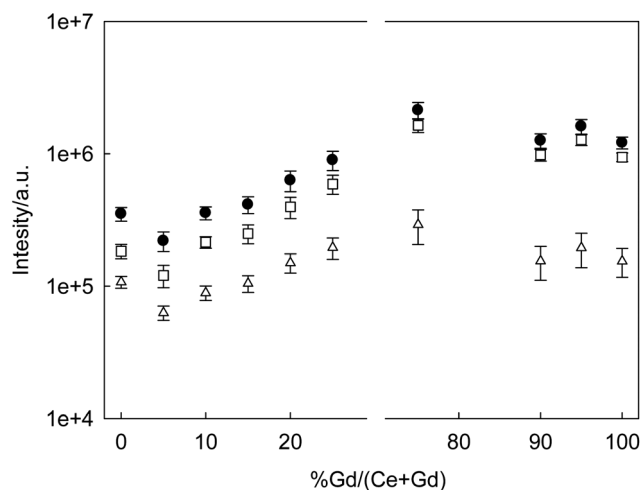


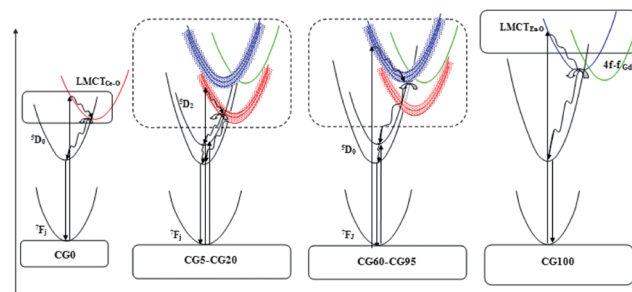
Fig. 11 Intensity of Eu(III) emission bands $5D_0 \rightarrow 7F_2$ (□) and $5D_0 \rightarrow 7F_1$ (Δ) and the sum of both (●), as a function of host composition ($\lambda_{\text{exc}} = 468$ nm).

$5D_0/7F_2$, $5D_0/7F_1$ and the sum of both as a function of the host composition.

Configurational coordinates

The sequence of excitation, relaxation, and emission processes in the samples can be interpreted in terms of the configurational coordinate model (Scheme 1). In the case of CG0, the excitation of Eu(III) takes place from the bottom of the $7F_0$ curve, rising along the straight vertical line, until it crosses the charge-transfer state of the LMCT Ce–O. Relaxation occurs along the LMCT curve and the excitation energy is transferred to $5D_J$ manifold to finally relax non-radiatively to the bottom of the $5D_0$ state followed by emission to $7F_J$ states.⁴⁰ In the case of CG100, the excitation energy is absorbed by the LMCT from the O^{2-} valence band at the bottom of the $7F_0$ curve rising along the straight vertical line to the Gd(III) conduction band at 234 nm (42735 cm^{-1}). The energy can be directly transferred to the $5D_J$ manifold of Eu(III), or to the LMCT Eu–O ($38314\text{ cm}^{-1} = 261\text{ nm}$). A similar route can be taken by direct excitation of the LMCT Eu–O: the energy can be transferred to the $5D_J$ manifold of Eu(III) or to the intra f–f $6I_J$ excited states of the Gd(III) ions ($276\text{ nm} = 36232\text{ cm}^{-1}$) before reaching the $5D_J$ manifold of Eu(III) to relax radiatively to the $7F_J$ states. Experimentally, it is observed that the energy transfer from the LMCT Eu–O band at 261 nm to the excited states of the Eu(III) ion in this matrix is the most efficient mechanism to sensitize the emission of Eu(III). The band gap of the Gd_2O_3 lies much higher in energy than the LMCT Eu–O and the intra f–f Gd(III) excited states.

Concerning the binary hosts, when 5% Ce(IV) is added to Gd_2O_3 , the excitation spectrum of CG95 shows that the intensity of the broad band centered at 261 nm of the Gd_2O_3 decreases remarkably with respect to CG100 (refer to Fig. 7 and 8). For CG90, this band is already absent while the broad band of CeO_2 (LMCT_{O–Ce}) increases very slightly shifting from 325 nm to 368 nm in CG0. The fact that the broad band centered at 261 nm is absent in the excitation spectra of these mixtures



Scheme 1 Illustration of a configurational coordinate model for end members CG0, CG100 and two representative CeO_2 -like and Gd_2O_3 -like ternary phosphors. The boxes represent the conduction and valence bands of each system.

($\lambda_{\text{em}} = 612\text{ nm}$) means that the energy is not being efficiently transferred from the LMCT Eu–O of the host to the $5D_J$ manifold of Eu(III) or to the intra f–f $6I_J$ excited states of the Gd(III) ions before reaching the $5D_J$ manifold of Eu(III) to relax radiatively to the $7F_J$ states.

As the oxides become richer in Ce(IV), the LMCT_{Ce–O} band enhances at the expense of a decrease in the intra 4f–f bands of the Eu(III) ion, the intensity of the band associated with the $5D_2 \rightarrow 7F_0$ transition being always higher in the excitation spectra of all the mixtures.

The excitation energy can be absorbed from the bottom of the $7F_0$ curve rising along the straight vertical line to the LMCT_{Ce–O}, and transferred to the $5D_J$ states of Eu(III) to relax radiatively to its $7F_J$ manifold. Alternatively, the most efficient is the direct excitation of the samples from the bottom of the $7F_0$ curve to the excited $5D_2$ level of the Eu(III) ion, with no matrix assistance. In fact, the LMCT_{Ce–O} band lies at much lower energy values than the bands associated with the Gd_2O_3 host, and therefore it crosses the excited $5D_0$ manifold of Eu(III) at lower energies. The results show that for the present level of Eu(III) dopant concentration in the mixtures, the band from the higher excited level $7F_0 \rightarrow 5D_2$ at 468 nm is present in all the excitation spectra and enhances as the samples become richer in ceria up to CG20 with the direct excitation of the Eu(III) being the most efficient way to obtain the most intense emission spectra.

For both families, the partial substitution of host cations dramatically decreases the efficiency of LMCT based emission, with respect to their respective end members (CG0 and CG100). In contrast, straight excitation of Eu(III) with visible light is enhanced with respect to them, once the host is partially substituted. Just considering the end members, CG100 offers emission intensities as high as 5 times of that exhibited by CG0. However, a CeO_2 -like rich host dramatically improves this value with the highest Gd(III) content (sample CG20), almost reaching the value of CG100.

Conclusions

Monodispersed spheroidal sub-microparticles obeying the general formula $Ce_{0.95-x}Gd_xEu_{0.05}O_{1.975-x/2}$, with $0 \leq x \leq 0.95$, were obtained by the urea method coupled with a high temperature oxidative annealing. Samples with $0.57 \leq x \leq 0.95$

exhibit a c-type structure while a $Fm\bar{3}m$ -type structure was found for $0 \leq x \leq 0.19$. For both ternary families, the partial substitution of host cations dramatically decreases the efficiency of the ligand to metal charge transfer (LMCT) based emission, with respect to their binary end members. The present Eu(III) based phosphors offer the possibility to be used as bio-probes given their ability to be excited at non-harmful radiation ranges. For both structures, the binary Ce(IV)–Gd(III) host improved emission with respect to $Gd_{0.95}Eu_{0.05}O_{1.5}$ and $Ce_{0.95}Eu_{0.05}O_{1.975}$ hosts, achieving an optimum value for the sample $Ce_{0.23}Gd_{0.71}Eu_{0.05}O_{1.6}$ with a $Ia\bar{3}$ structure.

Acknowledgements

This work was supported by grants CONICET PIP 11220110101020 and UBACYT 20020100100636. B.B. and M.J. are members of CONICET.

References

- 1 Y. Liu, D. Tu, H. Zhu, E. Ma and X. Chen, *Nanoscale*, 2013, **5**, 1369–1384.
- 2 S. Lechevallier, P. Lecante, R. Mauricot, H. Dexpert, J. Dexpert-Ghys, H. K. Kong, G. L. Law and K. L. Wong, *Chem. Mater.*, 2010, **22**, 6153–6161.
- 3 B. K. Gupta, T. N. Narayanan, S. A. Vithayathil, Y. Lee, S. Koshy, A. L. M. Reddy, A. Saha, V. Shanker, V. N. Singh, B. A. Kaiparettu, A. A. Marti and P. M. Ajayan, *Small*, 2012, **8**, 3028–3034.
- 4 S. Setua, D. Menon, A. Asok, S. Nair and M. Koyakutty, *Biomaterials*, 2010, **31**, 714–729.
- 5 J. G. Li, X. D. Li, X. D. Sun and T. Ishigaki, *J. Phys. Chem. C*, 2008, **112**, 11707–11716.
- 6 J. Chen, S. Patil, S. Seal and J. F. McGinnis, *Nat. Nanotechnol.*, 2006, **1**, 142–150.
- 7 E. G. Heckert, A. S. Karakoti, S. Seal and W. T. Self, *Biomaterials*, 2008, **29**, 2705–2709.
- 8 A. Karakoti, S. Singh, J. M. Dowding, S. Seal and W. T. Self, *Chem. Soc. Rev.*, 2010, **39**, 4422–4432.
- 9 S. K. Shi, M. Hossu, R. Hall and W. Chen, *J. Mater. Chem.*, 2012, **22**, 23461–23467.
- 10 J. G. Li, X. D. Li, X. D. Sun, T. Ikegami and T. Ishigaki, *Chem. Mater.*, 2008, **20**, 2274–2281.
- 11 L. F. Hu, R. Z. Ma, T. C. Ozawa and T. Sasaki, *Angew. Chem., Int. Ed.*, 2009, **48**, 3846–3849.
- 12 C. Wu, W. Qin, G. Qin, D. Zhao, J. Zhang, S. Huang, S. Lu, H. Liu and H. Lin, *Appl. Phys. Lett.*, 2003, **82**, 520–522.
- 13 A. Vecht, C. Gibbons, D. Davies, X. Jing, P. Marsh, T. Ireland, J. Silver, A. Newport and D. Barber, *J. Vac. Sci. Technol., B: Microelectron. Nanometer Struct.*, 1999, **17**, 750–757.
- 14 X. Jing, T. Ireland, C. Gibbons, D. J. Barber, J. Silver, A. Vecht, G. Fern, P. Trowga and D. C. Morton, *J. Electrochem. Soc.*, 1999, **146**, 4654–4658.
- 15 G. Soler-Illia, M. Jobbagy, R. J. Candal, A. E. Regazzoni and M. A. Blesa, *J. Dispersion Sci. Technol.*, 1998, **19**, 207–228.
- 16 E. Matijevic and W. P. Hsu, *J. Colloid Interface Sci.*, 1987, **118**, 506–523.
- 17 B. Aiken, W. P. Hsu and E. Matijevic, *J. Am. Ceram. Soc.*, 1988, **71**, 845–853.
- 18 T. C. Rojas and M. Ocana, *Scr. Mater.*, 2002, **46**, 655–660.
- 19 M. Jobbagy, C. Sorbello and E. E. Sileo, *J. Phys. Chem. C*, 2009, **113**, 10853–10857.
- 20 M. Jobbagy, F. Marino, B. Schobrod, G. Baronetti and M. Laborde, *Chem. Mater.*, 2006, **18**, 1945–1950.
- 21 M. Jobbagy, G. Soler-Illia, A. E. Regazzoni and M. A. Blesa, *Chem. Mater.*, 1998, **10**, 1632–1637.
- 22 J. G. Li, T. Ikegami, T. Mori and T. Wada, *Chem. Mater.*, 2001, **13**, 2921–2927.
- 23 J. G. Li, T. Ikegami, T. Mori and T. Wada, *Chem. Mater.*, 2001, **13**, 2913–2920.
- 24 W. Y. Hernandez, M. A. Centeno, F. Romero-Sarria and J. A. Odriozola, *J. Phys. Chem. C*, 2009, **113**, 5629–5635.
- 25 L. Armelao, D. Barreca, G. Bottaro, A. Gasparotto, E. Tondello, M. Ferroni and S. Polizzi, *Chem. Vap. Deposition*, 2004, **10**, 257–264.
- 26 P. Shuk, M. Greenblatt and M. Croft, *J. Alloys Compd.*, 2000, **303**, 465–471.
- 27 R. D. Shannon, *Acta Crystallogr., Sect. A: Cryst. Phys., Diffraction, Theor. Gen. Crystallogr.*, 1976, **32**, 751–767.
- 28 A. M. Pires, M. R. Davolos, C. O. Paiva-Santos, E. B. Stucchi and J. Flor, *J. Solid State Chem.*, 2003, **171**, 420–423.
- 29 T. Nakagawa, T. Osuki, T. A. Yamamoto, Y. Kitauji, M. Kano, M. Katsura and S. Emura, *J. Synchrotron Radiat.*, 2001, **8**, 740–742.
- 30 S. Babu, A. Schulte and S. Seal, *Appl. Phys. Lett.*, 2008, **92**, 123112.
- 31 Z. Wang, Z. Quan and J. Lin, *Inorg. Chem.*, 2007, **46**, 5237–5242.
- 32 T. Montini, A. Speghini, L. De Rogatis, B. Lorenzut, M. Bettinelli, M. Graziani and P. Fornasiero, *J. Am. Chem. Soc.*, 2009, **131**, 13155–13160.
- 33 M. Mogensen, N. M. Sammes and G. A. Tompsett, *Solid State Ionics*, 2000, **129**, 63–94.
- 34 H. Inaba and H. Tagawa, *Solid State Ionics*, 1996, **83**, 1–16.
- 35 S. Sen, H. J. Avila-Paredes and S. Kim, *J. Mater. Chem.*, 2008, **18**, 3915–3917.
- 36 N. J. Kim and J. F. Stebbins, *Chem. Mater.*, 2007, **19**, 5742–5747.
- 37 H. Deguchi, H. Yoshida, T. Inagaki and M. Horiuchi, *Solid State Ionics*, 2005, **176**, 1817–1825.
- 38 F. Ye, T. Mori, D. R. Ou, J. Zou, G. Auchterlonie and J. Drennan, *Solid State Ionics*, 2008, **179**, 827–831.
- 39 G. Blasse, A. Bril and W. C. Nieuwpoort, *J. Phys. Chem. Solids*, 1966, **27**, 1587–1592.
- 40 X. H. Liu, S. J. Chen and X. D. Wang, *J. Lumin.*, 2007, **127**, 650–654.
- 41 L. Li, H. K. Yang, B. K. Moon, Z. Fu, C. Guo, J. H. Jeong, S. S. Yi, K. Jang and H. S. Lee, *J. Phys. Chem. C*, 2009, **113**, 610–617.
- 42 M. Nakayama and M. Martin, *Phys. Chem. Chem. Phys.*, 2009, **11**, 3241–3249.
- 43 H. Yoshida, H. Deguchi, K. Miura, M. Horiuchi and T. Inagaki, *Solid State Ionics*, 2001, **140**, 191–199.
- 44 X. Wei, W. Pan, L. Cheng and B. Li, *Solid State Ionics*, 2009, **180**, 13–17.

- 45 C. Tiseanu, V. I. Parvulescu, M. Sanchez-Dominguez and M. Boutonnet, *J. Appl. Phys.*, 2012, **112**, 013521.
- 46 A. Kumar, S. Babu, A. S. Karakoti, A. Schulte and S. Seal, *Langmuir*, 2009, **25**, 10998–11007.
- 47 L. Li, H. K. Yang, B. K. Moon, Z. L. Fu, C. F. Guo, J. H. Jeong, S. S. Yi, K. Jang and H. S. Lee, *J. Phys. Chem. C*, 2009, **113**, 610–617.
- 48 M. Buijs, A. Meyerink and G. Blasse, *J. Lumin.*, 1987, **37**, 9–20.